Article

Convergence of coupling-parameter expansion-based solutions to Ornstein-Zernike equation in liquid state theory

S. V. G. MENON [1 †] *

[1] ShivEnclave, 304, 31-B-Wing, Tilak Nagar, Mumbai, India, 400089; menon.svg98@gmail.com
* Correspondence: menon.svg98@gmail.com; Tel.: +918879394488
† Retired from Bhabha Atomic Research Centre, Mumbai, India, 400085

Abstract: The objective of this paper is to investigate the convergence of coupling-parameter expansion-based solutions to Ornstein-Zernike equation in liquid state theory. The analytically solved Baxter's adhesive hard sphere model is analyzed first using coupling-parameter expansion. It is found that the expansion provides accurate approximations to solutions - including the liquid-vapor phase diagram - in most parts of the phase plane. However, it fails to converge in the region where the model has only complex solutions. Similar analysis and results are, then, obtained using analytical solutions within the mean spherical approximation for the hard-core Yukawa potential. Next, convergence of the expansion is analyzed for the Lennard-Jonnes potential using an accurate density-dependent bridge function in the closure relation. Numerical results are presented which show convergence of correlation functions, compressibility versus density profiles, etc., in the single as well as two phase regions. Computed liquid-vapor phase diagrams, using two independent schemes employing the converged profiles, compare excellently with simulation data. Results obtained for the generalized Lennard-Jonnes potential, with varying repulsive exponent, also compare well with simulation data. All these results together establish the coupling-parameter expansion as a practical tool for studying single component fluid phases modeled via general pair-potentials.

Keywords: Ornstein-Zernike equation; coupling-parameter expansion; thermodynamic perturbation theory; adhesive hard-sphere model; liquid-vapor phase transition; generalized Lennard-Jonnes potential.

1. Introduction

Liquid state theory deals with correlation functions, such as the pair-distribution function, to describe the structural and thermodynamics properties of fluids [1]. The correlation functions also form the basis in the modern theory of phase transitions in fluid systems [2]. The Ornstein-Zernike equation (OZE), which relates the direct and total correlation functions, is known to have excellent predictive power when supplemented with appropriate closure relations. The latter, as the name suggests, relates the two correlation functions and the interaction pair-potential. Although there are no exact closure relations, very accurate relations available in the literature provide results which compare excellently with those from computer simulations for homogeneous fluids [3].

For realistic interaction potentials and accurate closure relations, the OZE is a highly non-linear integral equation, which is numerically solved using Newton's method [4]. This approach works quite effectively for the case of purely repulsive interaction potentials [5]. However, a number of investigations show that the situation is quite different below the liquid-vapor phase transition temperature, which arises whenever there is an attractive component in the potential. Even simple

models show the occurrence of multiple solutions and 'no-real-solution-region' in the liquid-vapor coexistence region [6]. This feature is most clearly illustrated in Baxter's analytical solution of the adhesive hard sphere (AHS) model [7], which shows multiple solutions with even diverging pair distribution function. The model employs the Percus-Yevic (PY) closure for hard spheres with adhesion. The proper solution branch from multiple solutions is easily selected so as to satisfy the ideal gas limit and spatial convergence of the pair distribution function. However, the model shows the emergence of a density domain in the two-phase region where all solutions are complex. It also shows the absence of a true spinodal-line on the vapor side of the phase plane. Numerical methods also show similar features for the Lennard-Jones (LJ) potential and several important closure relations [8]. However, it is difficult to enumerate all solution branches with any numerical scheme. On the other hand, analytical solutions within the mean spherical approximation (MSA) for the hard-core Yukawa (HCY) potential show the occurrence of two real and two complex solutions in the entire phase-plane. More specifically, it is found that there is a domain in the two-phase region where all solutions are complex. The model shows proper spinodal-lines on vapor and liquid sides [9], as in van der Waals model and other mean field theories. Fortunately, the 'no-real-solution-region' in all models occurs inside the liquid-vapor coexistence dome, and careful strategies can be designed to map out the boundaries of the dome from numerical solutions of OZE [10].

An alternate approach to obtain useful approximations to fluid correlation functions is thermodynamic perturbation theory (TPT) [11]. Here, the basic idea is to use the known (or accurately calculable) solutions for a reference potential, and incorporate the effects of perturbing potential via correction terms. Perturbation theories based purely on the fluid free energy mostly use the hard sphere model as the reference system [12]. This is because of the availability of simulation data on hard sphere systems in very accurate parameter forms [11]. While first order correction terms are easily computed using the pair distribution function of the hard sphere system, three and four particle correlation functions are needed even for second order term. So the conventional TPT is restricted to low orders. The possibility to use the OZE in higher order perturbation theory avoids the requirement of complicated correlation functions, however, needs computation of higher order derivative terms of the correlation functions [13]. A systematic development of this approach, called coupling-parameter expansion (CPE), to arbitrary high orders has provided good results for model systems, in comparison to simulation data [14]. One of the most appropriate divisions of molecular potentials to reference and perturbing parts is based on the Weeks-Chandler-Anderson (WCA) prescription [15]. Recently, the CPE employing this division, and also incorporating density-dependent bridge functions, is developed as a general method, making use of efficient Newton-Armijo and Krylov space-based solvers [16]. It has been also applied to compute phase diagrams of metallic fluids using effective pair-potentials derived from cohesive energy curves. However, there remains an important issue related to convergence of the CPE.

The main objective of the paper is to obtain results on convergence of CPE, particularly in the two-phase region where OZE shows the occurrence of complex solutions. In what follows, CPE is first described briefly. Subsequently, its convergence is analyzed using the analytical solutions for AHS and HCY systems. Important conclusions on convergence are obtained in this manner. Then, numerical results are obtained using the general scheme for the LJ potential, which show convergence near the critical isotherm, and even in the two-phase region. Phase diagram of the LJ system is obtained via two independent schemes. Finally, the method is applied to generate the phase-diagrams for the general LJ(n,6) potentials, and compared with simulation data. The overall conclusion emerging from this analysis is that CPE is a practical approach for obtaining thermodynamic properties of one-component fluids, interacting via general potentials. It is hoped that CPE would find good use in generating equation of state data [17] in the fluid domain, which have important applications in high pressure physics.

2. Coupling-parameter expansion - General

The first step in introducing the general CPE [16] is to divide the inter-particle potential $U(r)$ into a reference (purely repulsive) and perturbation (purely attractive) components employing the the WCA prescription [15]. These components are given by:

$$\begin{aligned} U_0(r) &= U(r) - U_{min} \,, \quad r \leq r_{min} \,, \\ &= 0 \,, \qquad\qquad\quad r > r_{min} \,, \\ U_a(r) &= U_{min} \,, \qquad\quad r \leq r_{min} \,, \\ &= U(r) \,, \qquad\quad r > r_{min} \,. \end{aligned} \tag{1}$$

Here U_{min} denotes the potential-minimum at position r_{min}. The purely repulsive repulsive part U_0 determines the structure of dense liquids while the attractive perturbing component U_a gives rise to cohesion and phase changes [15]. When the coupling-parameter λ is introduced into the potential, it reads as $U(r,\lambda) = U_0(r) + \lambda U_a(r)$. The magnitude of λ, which varies over $0 \leq \lambda \leq 1$, determines the strength of the perturbation; thus, $U(r,0)$ is the reference part and $U(r,1)$ the full potential. Now, all correlation functions which determine the structure and thermodynamic properties of the fluid are also to be considered as functions of λ. In TPT, these functions are expanded as Taylor's series in λ about their reference part. For example, the pair distribution function $g(r,\lambda)$ is expanded as:

$$g(r,\lambda) = \sum_{n=0}^{\infty} \frac{1}{n!} \lambda^n g_n(r) \,, \tag{2}$$

Here $g_0(r)$ is the reference system's pair distribution function and $g_n(r)$ $(1 \leq n < \infty)$ denotes the n^{th} derivatives of $g(r,\lambda)$ at $\lambda = 0$. Similar Taylor's series expansions are also assumed for other correlation functions: the direct correlation function $c(r,\lambda)$, the total correlation function $h(r,\lambda) = g(r,\lambda) - 1$, and the indirect correlation function $y(r,\lambda) = h(r,\lambda) - c(r,\lambda)$. The subscript 0 in these functions denotes their corresponding functions for the reference system. The basic assumption in CPE is that these expansions converge and the series can be truncated at a suitable order. Thus the main idea is that the contributions from the perturbing part of potential are accurately accounted via the derivatives like $g_n(r)$. While traditional perturbation theory is limited to the first two orders [11], the general formulation of CPE can incorporate quite higher order derivatives by taking recourse to the OZE.

The OZE defines the consistency relation between the short ranged direct correlation function $c(r,\lambda)$ and the long ranged total correlation function $h(r,\lambda)$. The latter is the appropriate function to be used in the OZE as it tends to zero for large r, just like the pair-potential. For one-component systems modeled using spherically symmetric potentials, the OZE is written as:

$$h(r,\lambda) = c(r,\lambda) + \rho \int c(|\vec{r} - \vec{r'}|,\lambda)\; h(r',\lambda)\; d\vec{r'}. \tag{3}$$

where ρ is the number density of fluid particles. This is one equation in two unknowns, and so need to be supplemented with a closure relation involving $h(r,\lambda)$, $c(r,\lambda)$ and the pair-potential $U(r,\lambda)$. An exact closure is unfeasible, however, several approximate forms are available [1]. All the closures are generally expressed concisely in terms of a 'bridge function' $B(r,\lambda)$ in the form:

$$c(r,\lambda) = \exp[-\beta U(r,\lambda) + y(r,\lambda) + B(r,\lambda)] - y(r,\lambda) - 1 \,, \tag{4}$$

where $\beta = (k_B T)^{-1}$, k_B is Boltzmann's constant and T absolute temperature. Approximate forms of $B(r,\lambda)$ generate different closures; for instance, $B(r,\lambda) = \ln[1 + y(r,\lambda)] - y(r,\lambda)$ yields the PY closure

while the hypernetted-chain closure (HNC) is obtained with $B(r,\lambda) = 0$. A bridge function applicable to general potentials [18] is:

$$\begin{aligned} B(r,\lambda) &= \sqrt{1+2\,\omega(r,\lambda)} - \omega(r,\lambda) - 1\,, \\ \omega(r,\lambda) &= y(r,\lambda) - \lambda\rho\beta U_a(r)\,. \end{aligned} \tag{5}$$

which will be used throughout the present paper. This function has been shown to provide accurate thermodynamic properties for hard sphere as well as LJ systems .

2.1. Method of solution

The solution of integral equation Eq.(3), with a displacement kernel, in Fourier space is easily expressed as:

$$\bar{y}(k,\lambda) = \frac{\rho\bar{c}^2(k,\lambda)}{1-\rho\bar{c}(k,\lambda)}\,, \tag{6}$$

where the Fourier transform (denoted with a 'bar' throughout) and its inverse, for any function $q(r)$, are defined as

$$\begin{aligned} k\,\bar{q}(k) &= 4\pi\int_0^\infty \sin(kr)\; r\; q(r)\; dr\,, \\ r\; q(r) &= (2\pi^2)^{-1}\int_0^\infty \sin(kr)\; k\; \bar{q}(k)\; dk\,. \end{aligned} \tag{7}$$

The algebraic equations Eqs.(4) and (6), although the first is defined in r-space and the second in k-space, define a closed non-linear system within the integral equation formalism. Different implementations of Newton's method to solve this system is now well developed [19]. However, all have to deal with problems, mentioned earlier, related to 'no-real-solution-region' in the two-phase region.

In CPE, the Newton-Armijo solver is employed only for determining correlation functions of reference-part. Starting with an initial guess y_0 (and hence c_0, $\bar{c}_0$ and $\bar{y}_0$), a correction Δy is obtained by solving the linear system [16]:

$$\Delta\bar{y} = \rho\frac{2\bar{c}_0+\bar{y}_0}{1-\rho\bar{c}_0}\overline{\Big[(h_0+g_0\Lambda_0)\Delta y\Big]} + \Big[\rho\frac{\bar{c}_0^2}{1-\rho\bar{c}_0} - \bar{y}_0\Big]\,. \tag{8}$$

Here $\Lambda_0 = [1+2y_0]^{-1/2} - 1$ is the derivative $\partial B/\partial y$ at $\lambda = 0$. Fourier transforms and inverses are computed using FFT (fast-Fourier-transform) algorithms. The linear system implicitly defined in Eq.(8) is best solved with Krylov space-based methods like CGNR (Conjugate Gradient to Normal equations to minimize Residual) or GMRES (Generalized Minimum Residual). This is so because it is possible to perform matrix-vector products via two Fourier transform operations. Armijo scheme is used to limit the correction $\Delta\bar{y}$ to $\xi\Delta\bar{y}$ with $0 < \xi < 1$ in case error reduction does not occur at any iteration.

The derivatives of correlation functions are obtained from the solutions of the linear system:

$$\bar{y}_n = [\bar{s_0}^{\,2} - 1]\overline{\Big[(h_0+g_0\Lambda_0)y_n\Big]} + [\bar{s_0}^{\,2} - 1]\bar{w}_n + \bar{q}_n\,, \quad n \geq 1\,. \tag{9}$$

Here, $\bar{s}_0 = [1 - \rho\bar{c}_0]^{-1}$ denotes the structure factor of the reference system. Denoting the derivatives of the bridge function also as $B_n = \Lambda_0 y_n + B^*_n$, the source terms, viz., w_n and $\bar{q}_n$, are given by:

$$\begin{aligned} w_n &= -g_0\beta U_a\delta_{n\,1} + g_0 B^*_n + \sum_{m=1}^{n-1} C^{n-1}_m \left[-\beta U_a\delta_{n-m,\,1} + y_{n-m} + B_{n-m}\right]\left[y_m + c_m\right] ,\ n \geq 1 . \\ \bar{q}_n &= \bar{s}_0 \sum_{m=1}^{n-1} C^n_m\, \bar{c}_{n-m}\, \rho[\bar{y}_m + \bar{c}_m] ,\ n \geq 1. \end{aligned} \tag{10}$$

Here C^n_m denotes the binomial coefficient. Note that these terms involve only lower order derivatives, and hence are known at nth order. Further, the linear operator in Eq.(9) (for all orders) is identical to that in Eq.(8). Finally, the derivatives B^*_n are expressed as:

$$\begin{aligned} B^*_n &= -\Lambda_0\beta\rho U_a\delta_{n\,1} - (1+\Lambda_0)\sum_{m=0}^{n-2} C^{n-1}_m \mathcal{O}_{m+1}\mathcal{O}_{n-1-m} ,\ n \geq 1 , \\ \mathcal{O}_n &= (1+\Lambda_0)y_n + B^*_n ,\ n \geq 1. \end{aligned} \tag{11}$$

As the summation contributes only for $n \geq 2$, this equation provides B^*_n explicitly at all orders. Derivations of these expressions are given in detail in the recent formulation of CPE mentioned earlier [16]. Concise algorithms for implementing the complete CPE method are also discussed there. (The line $l = l$ in Algorithm A5, provided in this reference, should be corrected as $l = 2\ l$.)

2.2. Thermodynamic functions

Once the derivatives are determined to the required order, explicit expressions for the correlation functions follow as functions of λ. Then, the series for $g(r,\lambda)$ provides an explicit expression for free energy F per particle [20] :

$$\beta F(\rho,T) = \beta F_0(\rho,T) + \frac{\rho}{2}\int d\vec{r}\int_0^1 d\lambda\ \beta U_a(r)\ g(r,\lambda) . \tag{12}$$

Here F_0 is free energy per particle of the reference system. With the series expansion for $g(r,\lambda)$, the integral term over λ is evaluated as $\sum_{n=0}^{\infty}\ g_n/(n+1)!$. Using the closure relation, which is also expressed as: $g(r,\lambda) = \exp[-\beta U(r,\lambda) + y(r,\lambda) + B(r,\lambda)]$, the above expression is recast as [20]

$$\begin{aligned} \beta F(\rho,T) &= \beta F_0(\rho,T) + \frac{\rho}{2}\int d\vec{r}\left[-g_a(r,1) + g(r,1)(y_a(r,1) + B_a(r,1))\right] \\ &- \frac{\rho}{2}\int d\vec{r}\int_0^1 d\lambda\ \left[y_a(r,\lambda) + B_a(r,\lambda)\right]\left[\partial\ g_a(r,\lambda)/\partial\lambda\right] . \end{aligned} \tag{13}$$

Here the subscript in $g_a(r,\lambda)$ (and similarly other functions) denotes the excess contribution over that of the reference potential, i.e., $g(r,\lambda) \equiv g_0(r) + g_a(r,\lambda)$. This form does not involve the attractive potential explicitly. Again, the integral term over λ is obtained as $\sum_{n=1}^{\infty}\ g_n/(n-1)!\sum_{m=1}^{\infty}\ (y_m + B_m)/[(n+m)m!]$. Once $F(\rho,T)$ is determined, pressure $\beta P = \rho^2(\partial F/\partial\rho)_T$ and chemical potential $\beta\mu = \beta F + \beta P/\rho$ are readily computed.

Thermodynamic properties are also be obtained via the compressibility route. The (reduced) inverse compressibility χ^{-1} is given in terms of direct correlation function as:

$$\chi^{-1} = \beta(\partial P/\partial\rho)_T = 1 - 4\pi\rho\int_0^{\infty} c(r,1)\ r^2 dr . \tag{14}$$

As the function $c(r,1)$ is short ranged, χ^{-1} is the most appropriate response function to compute pressure on an isotherm via integration with respect to ρ, whenever possible. The chemical potential μ is also determined by integrating the thermodynamic equation $\rho(\partial\mu/\partial\rho)_T = (\partial P/\partial\rho)_T$:

$$\beta\mu = \ln(\rho) + 3\ln(\lambda_{th}) + \int_0^\rho \frac{d\rho}{\rho}(\chi^{-1} - 1);. \tag{15}$$

The first two terms, where $\lambda_{th} = h/\sqrt{(2\pi m k_B T)}$ is the thermal wavelength, are the ideal gas contributions. This approach is always useful to compute $\beta F_0 = \beta\mu_0 - \beta P_0/\rho$ for the reference system. There are also explicit expressions for virial-pressure and chemical potential [10], involving $g(r,1)$, $c(r,1)$ and $B(r,1)$.

Having outlined the the general algorithm for CPE, numerical investigation of convergence of the expansion for specific potentials is readily carried out. Before that, this analysis is done using analytical solutions of two model problems in the next two sections.

3. Coupling parameter expansion - AHS model

Baxter's AHS model deals with a system of hard spheres (of diameter σ) with an infinitely narrow attractive square well potential (of width Δ) representing surface adhesion [7]. The well depth is taken as $\beta\phi = \ln[\tau\Delta/(\sigma+\Delta)]$, where the parameter τ represents an effective temperature, being zero at zero temperature and large at high temperature. In the limit $\Delta \to 0$, this particular form reduces Mayer's function to the form: $f(r) = -1 + (\sigma/12\tau)\delta(r-\sigma)$, where -1 represents the hard sphere contribution. Using virial expansion, it is also shown that the total correlation function reduces to $h(r) = -1 + (\Gamma\ \sigma/12\tau)\ \delta(r-\sigma)$ for the range $0 \le r \le \sigma$, where Γ is a parameter to be determined employing OZE and PY closure. Baxter showed that $\Gamma^* = \eta(1-\eta)\Gamma$ satisfies the quadratic equation:

$$\frac{1}{12}(\Gamma^*)^2 - [\tau(1-\eta)+\eta]\Gamma^* + \eta(1+\eta/2) = 0\,, \tag{16}$$

where $\eta = \pi\rho\sigma^3/6$ is the volume fraction of particles. This equation shows that the solutions are real in the entire range $0 < \eta < 1$ when $\tau > \tau_c = (2-\sqrt{2})/6 \approx 0.0976$. However, they turn complex for a range $\eta_1(\tau) < \eta < \eta_2(\tau)$ around $\eta_c = (3/\sqrt{2} - 2) \approx 0.1213$ when $\tau < \tau_c$. These boundaries are determined from the condition of vanishing discriminant in Eq.(16), viz., $[\tau(1-\eta)+\eta]^2 - (\eta/3)(1+\eta/2) = 0$. Thus the model predicts a gas-liquid phase transition with critical parameters τ_c and η_c. The proper root Γ^*, out of the two solutions, that satisfy the ideal gas limit (for small η) is the negative root given by:

$$\Gamma^* = 6[\tau(1-\eta)+\eta] - 6[(\tau(1-\eta)+\eta)^2 - (\eta/3)(1+\eta/2)]^{1/2}\,. \tag{17}$$

Analytical expression for pressure [7], obtained by integrating compressibility for $\tau > \tau_c$, and analytically continued to $\tau < \tau_c$ as well, is given by:

$$\beta\frac{P}{\rho} = \frac{1+\eta+\eta^2}{(1-\eta)^3} - \frac{\Gamma^*(2+\eta)}{2(1-\eta)^3} + \frac{\Gamma^{*3}}{36\eta(1-\eta)^3}\,. \tag{18}$$

Here the first term is compressibility-pressure for hard spheres with in PY closure. Other terms involving Γ^* are the contributions of surface adhesion. Similar expression for chemical potential is also derived [21], and these expressions facilitate determination of phase diagram [21] using thermodynamic conditions. It is nice to note that the 'no-real-solution-region', where Γ^* and hence P are undefined, is contained inside the co-existence region (see below). Equally important, the model shows the emergence of multiple solutions in all regions and a 'no-real-solution-region' in the two-phase region.

The equations of the AHS model are also derived as the lowest order solution to Baxter's factorized form of OZE [22]. This analysis employed $\epsilon = \Delta/(\sigma+\Delta)$ as a perturbation parameter [23], and

directly showed that Eq.(16) is accurate to $O(\epsilon)$ and the parameters Γ and τ are related to square well parameters as:

$$\tau = (12\,\epsilon)^{-1} \exp(\beta\, u_0)\,, \qquad \Gamma = 12 \int_{1-\epsilon}^{1} g[(\sigma+\Delta)\,x]\; x\; dx\,, \tag{19}$$

where $u_0 < 0$ is the depth of the potential. Now, all results of the model can be discussed in the usual phase-plane as the parameter τ is explicitly related to T .

The CPE is introduced by replacing the potential depth u_0 with λu_0. Then, the function $\tau(\lambda)$ and $\Gamma^*(\lambda)$, which is directly related to $\tau(\lambda)$, are expanded in power series as:

$$\tau(\lambda) = \sum_{n=0}^{\infty} \lambda^n\, \tau_n\,, \qquad \Gamma^*(\lambda) = \sum_{n=0}^{\infty} \lambda^n\, \Gamma_n^*\,. \tag{20}$$

The series for $\tau(\lambda)$ is uniformly convergent with expansion coefficients $\tau_n = (12\epsilon\; n!)^{-1}[\beta u_0]^n$ for $n \geq 0$. Substitution from Eqs.(20) into the quadratic equation, Eq.(16), yields the expansion coefficients Γ_n^*:

$$\begin{aligned} \Gamma_n^* &= \frac{\omega_n}{[\tau_0(1-\eta) - (1/6)\Gamma_0^* + \eta]}\,, \quad n \geq 1 \\ \omega_n &= \frac{1}{12} \sum_{m=1}^{n-1} \Gamma_m^*\, \Gamma_{n-m}^* - (1-\eta) \sum_{m=1}^{n} \tau_m\, \Gamma_{n-m}^*\,, \quad n \geq 1 \end{aligned} \tag{21}$$

where Γ_0^* satisfies an equation similar to Eq.(16), but with τ_0 in place of τ:

$$\frac{1}{12}(\Gamma_0^*)^2 - [\tau_0(1-\eta)+\eta]\Gamma_0^* + \eta(1+\eta/2) = 0\,. \tag{22}$$

This equation is similar to the OZE for reference potential while Eq.(21) is analogous to the solution of the linear system defined in Eq.(9). The coefficients Γ_n^* obtained up to sufficient order provides $\Gamma^*(1)$ which yield all thermodynamic properties within CPE. The series expansion for $\Gamma^*(\lambda)$ is also derivable from Eq.(17). However, by writing the second square bracket term in this expression as $\sqrt{1-x}$, where $x = (\eta/3)(1+\eta/2)/(\tau(1-\eta)+\eta)^2$, this equation shows that the series fails to converge for $\eta_1(\tau) < \eta < \eta_2(\tau)$ when $\tau < \tau_c$, that is, within the 'no-real-solution-region'. Thus, the real values of $\Gamma^*(1)$ obtained in this region, at any order of truncation, do not correspond to a convergent series. However, this is not a serious issue as discussed below.

Variation of $\Gamma^*(1)$ versus η is compared with exact solution (see Eq.(17)) in Fig.1A for two values of reduced temperature $T^* = k_B T/u_0$. These results correspond to the perturbation (width) parameter $\epsilon = 0.1$, which yields the critical temperature $T_c^* \approx 0.4663$. Lower part (for $T^* = 0.5$) shows $\Gamma^*(1)$ versus η, obtained using CPE of 20-th order (curve-1), and exact results (symbols). The two sets of results compare excellently, and this case corresponds to $T^* > T_c^*$. Similar comparison is found even at 10-th order. In the upper part (for $T^* = 0.4$) the range $\eta_1 < \eta < \eta_2$ is the 'no-real-solution-region'. Again, $\Gamma^*(1)$ versus η, from CPE of 20-th order (curve-2), and exact results (symbols) are shown in the graphs. There are deviations between the two sets of results in the neighborhood of η_1 and η_2, otherwise they agree quite well. Next, the phase diagram of AHS model is computed using the analytical expressions for P and μ in the thermodynamic conditions, viz., $P_L = P_G$ and $\mu_L = \mu_G$, where the subscripts L and G, respectively, denote the liquid and gaseous branches. Exact results for phase diagram (symbols) are compared in Fig.1B with those obtained using CPE of 50-th order (curve-2) and 20-th order (curve-3). These agree each other except close to the critical point. The 'no-real-solution-region', lying within the dashed lines (curve-1), is also shown. These comparisons show that CPE provides useful results because the 'no-real-solution-region', where the expansion fails to converge, lies completely inside the co-existence dome.

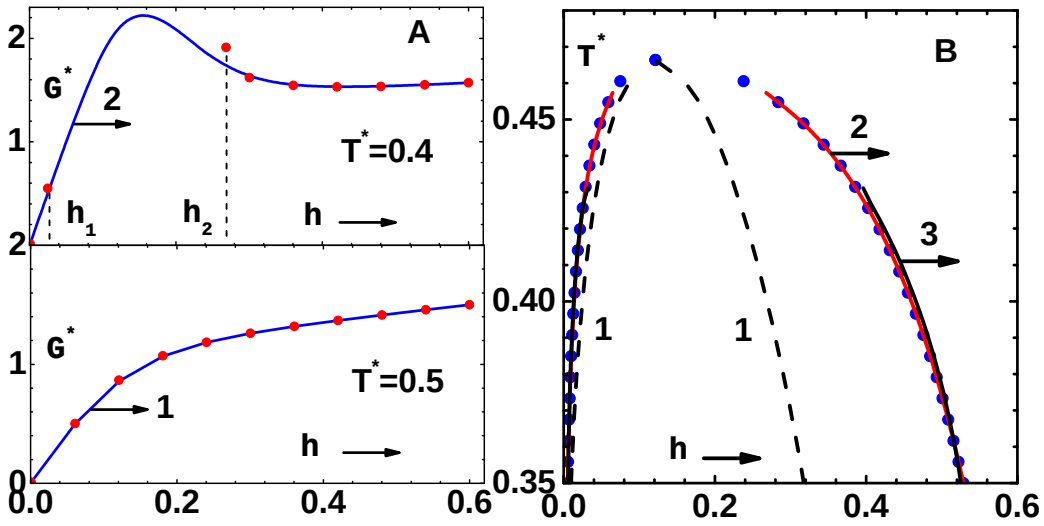

Figure 1. (**A**) Lower part ($for T^* = 0.5$) shows variation of $\Gamma^*(1)$, from CPE of 20-th order (curve-1), and exact results (symbols) versus η. In the upper part ($for T^* = 0.4$) the range $\eta_1 < \eta < \eta_2$ is the 'no-real-solution-region. Graphs show $\Gamma^*(1)$, from CPE of 20-th order (curve-1), and exact results (symbols) versus η. (**B**) Exact results for phase diagram of AHS model (symbols) compared with those obtained using CPE of 50-th order (curve-2) and 20-th order (curve-3). The 'no-real-solution-region', lying within the dashed lines (curve-1), is also shown.

4. Coupling parameter expansion - MSA model

System of hard spheres (of diameter σ) attached with attractive Yukawa potential is analytically solved within the MSA closure [24]. The Yukawa part, defined over the range $r \geq \sigma$, is expressed as $(-J\sigma/r)\exp[-\xi(r-\sigma)]$, where ξ and J are range and depth parameters, respectively. Analytical results of the model are useful to analyze the convergence properties of CPE. The central parameter Φ, which is used to express all the results of the model, satisfy the forth order equation [9]:

$$6\eta^2\Phi^4 - X\Phi^3 + 12\eta K\Phi^2 - KY\Phi + K^2 = 0\,, \tag{23}$$

where $K = \beta J$ and X and Y are functions of ξ. Note that this model has more solutions compared to the AHS model. This equation has two real and two complex solutions in the entire range of η for K (proportional to T^{-1}) lower than a critical value $K^*(\xi)$. Out of the two real solutions, the proper one must approach the ideal gas limit for small η, and also should vanish as $K \to 0$. For the region $K > K^*(\xi)$, there is a 'no-real-solution-region' for a range $\eta_1(\xi) < \eta < \eta_2(\xi)$, because all solutions turn complex. Thus the results of the model, although there are more solutions, are similar to those of AHS model. However, an important difference is that spinodal lines, which now occur on both the gaseous and liquid branches, cover the 'no-real-solution-region'. Thus the occurrence of the latter may not be of much consequence in determining the phase diagram.

The CPE is introduced in the model by replacing K with λK. Then the reference solution (for $\lambda = 0$) is that of hard spheres within the PY closure. As the proper real solution must approach zero as $\lambda \to 0$, the series expansion for $\Phi(\lambda)$ must start at first order, and is given by:

$$\Phi(\lambda) = \sum_{n=1}^{\infty} \lambda^n \, \phi_n \,. \tag{24}$$

Recursion relations for the expansion coefficients ϕ_n readily follow on substituting this series in Eq.(23):

$$\phi_1 = \frac{K}{Y}\,, \quad \phi_2 = \frac{12\eta K\psi_{2,2} - X\psi_{3,3}}{KY}\,, \quad \phi_n = \frac{12\eta K\psi_{2,n} - X\psi_{3,n+1} + 6\eta^2\psi_{4,n+1}}{KY}\,,\ n \geq 3\,, \tag{25}$$

where the additional coefficients $\psi_{2,n}$, $\psi_{3,n}$ and $\psi_{4,n}$ are obtained as:

$$\psi_{2,n} = \sum_{m=1}^{n-1} \phi_m\, \phi_{n-m}\,,\ n \geq 2\,;\ \psi_{3,n} = \sum_{m=1}^{n-2} \phi_m\, \psi_{2,n-m}\,,\ n \geq 3\,;\ \psi_{4,n} = \sum_{m=1}^{n-3} \phi_m\, \psi_{3,n-m}\,,\ n \geq 4\,. \tag{26}$$

After truncating the expansion at a suitable order, $\Phi(1)$ is to be substituted in the analytical expressions [9] to obtain the results within CPE. Note that CPE generates real solutions for all values of η and K.

The series solution $\Phi(1)$ versus η is compared with exact solutions, which are are simply the roots of Eq.(23), for two values of the parameter K in Fig.2A. These results are for the range parameter $\xi = 2$ which yields the critical value $K^* \approx 1.1354$. The lower part (for $K = 0.8$) shows $\Phi(1)$, obtained from CPE of 20-th order (curve-1) and exact results (curve-2). The latter is the real root of Eq.(23) discussed earlier. The two sets of results agree excellently, however, note that this case is in the region of K with two real solutions. The series solution converges quite fast, in fact, low order expansions (say 10-th order) also yield similar comparisons. In the upper part (for $K = 1.2 > K^*$), the range $\eta_1 < \eta < \eta_2$ is the 'no-real-solution-region'. Graphs show $\Phi(1)$, obtained from CPE of 20-th order (curve-1) and real (curve-2) and imaginary (curve-3) parts of the exact root. The CPE does not converge to the complex solutions, and there are also significant deviations outside the 'no-real-solution-region'. Exact results for (reduced) inverse compressibility χ^{-1} (curve-1), obtained using analytical expressions [9], are compared in Fig.2B with those obtained using CPE of 20-th order (curve-1). Note that exact values of χ^{-1} are complex in the 'no-real-solution-region'.

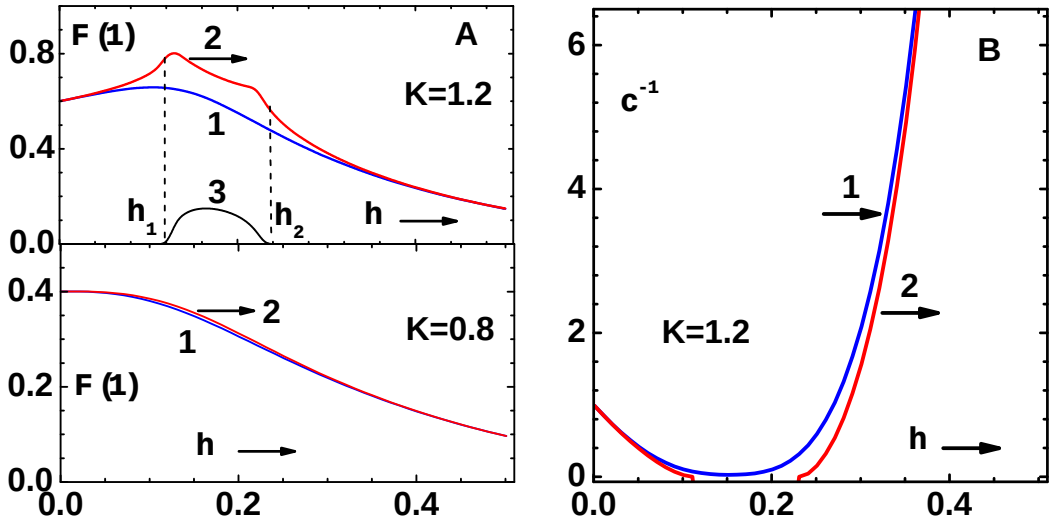

Figure 2. (**A**) Lower part (for $K = 0.8, \xi = 2$) shows $\Phi(1)$ versus η, obtained from CPE of 20-th order (curve-1), and exact results (curve-2). In the upper part (for $K = 1.2, \xi = 2$), the range $\eta_1 < \eta < \eta_2$ is 'no-real-solution-region, as $K^* \approx 1.1354$. Graphs show $\Phi(1)$ versus η, obtained from CPE of 20-th order (curve-1), and real (curve-2) and imaginary (curve-3) parts of exact results. (**B**) Graphs show (reduced) inverse compressibility χ^{-1} versus η , obtained from CPE (curve-1) and exact results [9] (curve-2) for $K = 1.2$.

The results presented above for the AHS and MSA models show several features: (i) The CPE converges to exact results quite well in regions of phase plane, where there are real solutions. (ii) The expansion fails to converge in 'no-real-solution region', which exists within both models. (iii) CPE is useful to derive the phase diagram, using thermodynamic conditions, if it totally contains (as in the AHS model) the 'no-real-solution region'.

5. Coupling parameter expansion - LJ potential

This section presents numerical results for the more realistic LJ potential: $U(r) = 4\epsilon[(\sigma/r)^{12} - (\sigma/r)^6]$, where ϵ and σ are, respectively, the depth and range parameters. The density-dependent bridge function given in Eq.(5) defines the closure relation for OZE. This is important because the predictive power of OZE depends solely on the accuracy of the bridge function. In obtaining numerical results, CPE (outlined earlier) is truncated at 7-th order, i.e., expansion including terms up to g_6, are used throughout the analysis. Reduced temperature $T^* = k_B T/\epsilon$ and density $\rho^* = \rho\sigma^3$ are the variables used, and the argument $\lambda = 1$ is omitted from different expressions.

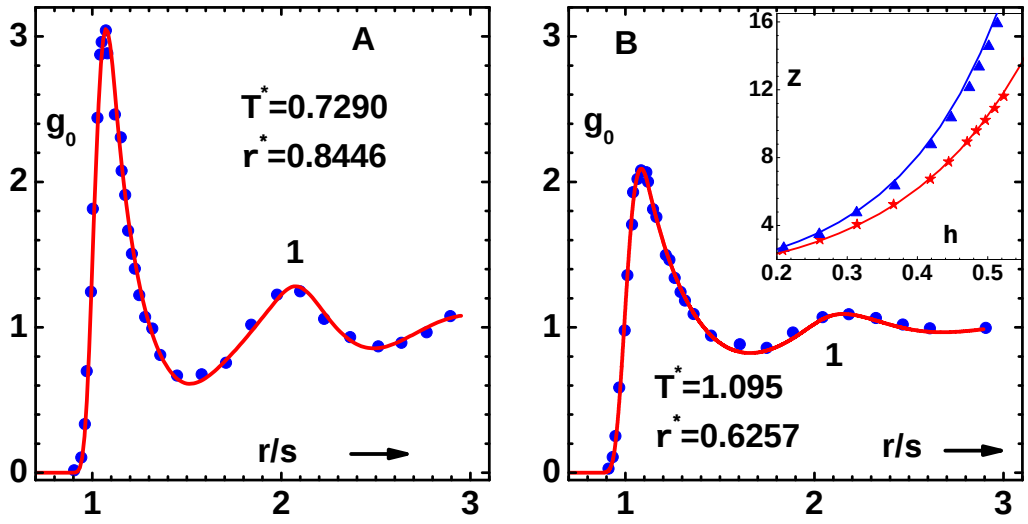

Figure 3. (**A**) Pair distribution function $g_0(r/\sigma)$ versus scaled distance (r/σ) (curve-1) for the reference system of LJ potential, as per the WCA prescription (see text), at reduced temperature $T^* = 0.7290$ and density $\rho^* = 0.8446$. Symbols are molecular dynamics simulation results [27]. (**B**) Similar results for the parameters $T^* = 1.095$ and density $\rho^* = 0.6257$. The inset figure shows compressibility factor $Z = \beta P/\rho$ versus volume fraction $\eta = \pi\rho^*/6$ for reduced temperature $T^* = 0.75$ (top curve) and $T^* = 2.0$ (bottom curve). Symbols are simulation results [28].

The CPE around $\lambda = 0$ provides real solutions throughout the phase plane if the series expansion converges. In the case of AHS and MSA models, discussed in previous sections, convergence is clearly evident above the gas-liquid phase transition temperature. However, for the more realistic model considered here, convergence can only be tested numerically at somewhat lower orders of expansions. The LJ model (and bridge function) is also analyzed by applying Newton's method to the full potential [8], where provisions to search for complex solutions are also builtin. This analysis reveals features similar to those found in AHS model, i.e., occurrence of a 'no-real-solution-line' on the gaseous side of an isotherm below critical temperate. Compressiblility is found to be finite, but complex, along this line but the constant-volume heat capacity diverges. Although there is no true spnodal line on the gaseous side, the same analysis has found one to the left of the co-existence line on the liquid

side. Emergence of complex isothermal compressibility, within the HNC closure, is also presented as a 'fold-bifurcation' [25] on isotherms for sub-critical temperatures. In fact, this feature is observed with several other closures [26], including the one considered here. However, the series expansion in CPE, about the repulsive component of the potential, will not pick up these complex solutions. But, as shown below, CPE is useful to compute the phase diagram, which encompasses the 'no-real-solution region', because it converges well outside this region.

First of all, it is necessary to check the accuracy of modeling the reference system resulting from WCA prescription. To that end, the pair distribution function $g_0(r/\sigma)$ versus scaled distance (r/σ) (curve-1), which corresponds to $T^* = 0.7290$ and $\rho^* = 0.8446$, is compared against molecular dynamics simulation data (symbols) [27] in Fig.3A. Similar comparison is shown in Fig.3B for the case $T^* = 1.095$ and $\rho^* = 0.6257$. Excellent agreement found in peak heights and variations in the entire range of (r/σ) demonstrates the accuracy of the bridge function for the repulsive WCA potential. The compressibility factor $Z = \beta P/\rho$ versus volume fraction, $\eta = \pi\rho^*/6$, is compared against simulation data (symbols) [28] in the insert figure for two temperatures: $T^* = 0.75$ (top curve) and $T^* = 2.0$ (bottom curve). Here also the agreement is quite good, although slight differences are noted at higher η for the low temperature case. All these results, obtained via the compressibility route, are found to be superior to those from the virial route.

Next, convergence of the correlation functions $c(r/\sigma)$ and $g(r/\sigma)$ is analyzed in Fig.4 for single phase region and Fig.5 for two phase region. The former figure corresponds to the phase point $\rho^* = 0.3$ and $T^* = 1.45$, which is above the critical temperature, while the latter one is for $\rho^* = 0.3$ and $T^* = 1.15$ lying within the the spinodal region (see below). In both figures, the left and right panels (A and B) correspond to $c(r/\sigma)$ and $g(r/\sigma)$, respectively. The functions $c(r/\sigma)$ (curve-c), the reference function $c_0(r/\sigma)$ (curve-0) and six successive derivative terms $c_n(r/\sigma)/n!$ (curve-1 to curve-6) are shown in both left panels. Similarly, the two right panels show $g(r/\sigma)$ (curve-g), the reference function $g_0(r/\sigma)$ (curve-0) and six successive derivative terms $g_n(r/\sigma)/n!$ (curve-1 to curve-6).

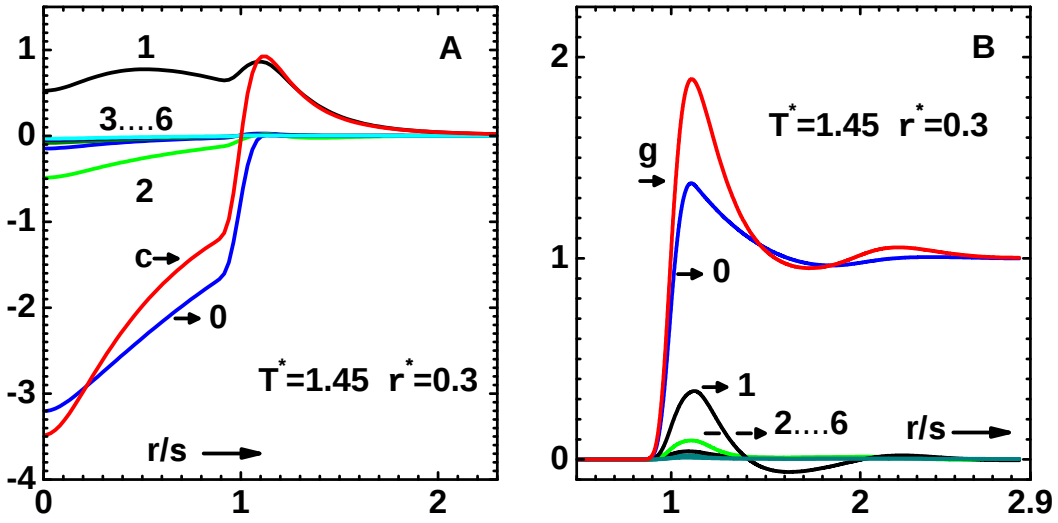

Figure 4. Convergence of direct correlation function $c(r/\sigma)$ and pair distribution function $g(r/\sigma)$ for the LJ system at the phase point $\rho^* = 0.3$ and $T^* = 1.45$, which is above critical temperature. (**A**) Graphs show $c(r/\sigma)$ (curve-c), reference function $c_0(r/\sigma)$ (curve-0) and successive derivative terms $c_n(r/\sigma)/n!$ (curve-1 to curve-6). (**B**) Similarly, the graphs show $g(r)$ (curve-g), reference function $g_0(r/\sigma)$ (curve-0) and derivative terms $g_n(r/\sigma)/n!$ (curve-1 to curve-6) for the same phase point.

Convergence to well defined functions, shown as $c(r/\sigma)$ and $g(r/\sigma)$, although based on numerical results, is evident at both phase points. Also, it is the first order term that contributes the main correction. Note that the reference function $c_0(r/\sigma)$ is negative at both phase points, however, graphs of $c(r/\sigma)$ for $r > \sigma$ have positive parts, which arise due to attractive interactions. This positive component is more pronounced at the spinodal region (Fig.5A), and it leads to negative compressibility at that point (see below). The reference functions $g_0(r/\sigma)$ have only small first peaks at both phase points. But, the first and second peaks in $g(r/\sigma)$ are more pronounced in the spinodal region (Fig.5B). This is because of lower temperature T^* at this point, which amplifies the effects of attractive interactions.

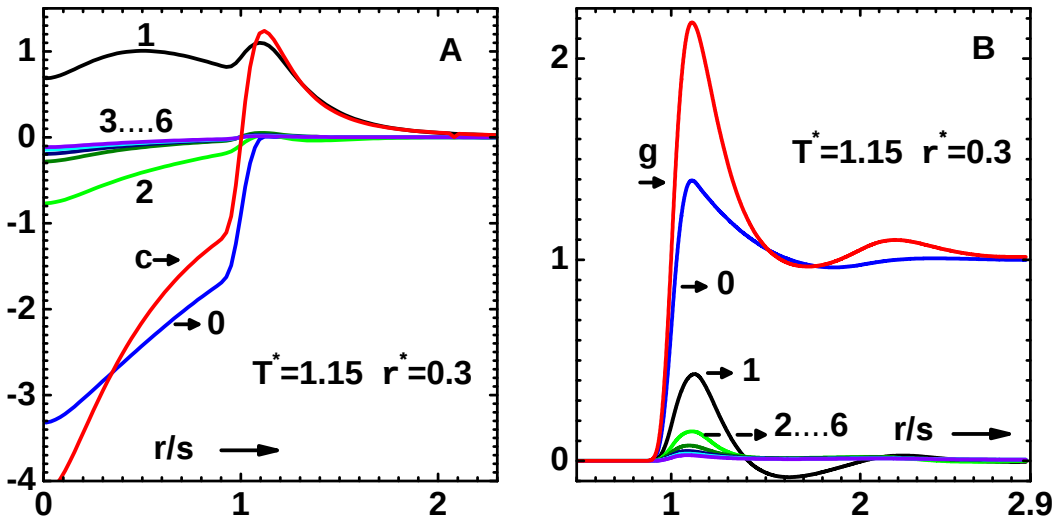

Figure 5. Convergence of direct correlation function $c(r/\sigma)$ and pair distribution function $g(r/\sigma)$ for the LJ system at the phase point $\rho^* = 0.3$ and $T^* = 1.15$, which is in the spinodal region. (**A**) Graphs show $c(r/\sigma)$ (curve-c), reference function $c_0(r/\sigma)$ (curve-0) and successive derivative terms $c_n(r/\sigma)/n!$ (curve-1 to curve-6). (**B**) Similarly, the graphs show $g(r/\sigma)$ (curve-g), reference function $g_0(r/\sigma)$ (curve-0) and derivative terms $g_n(r/\sigma)/n!$ (curve-1 to curve-6) for the same phase point.

Graphs of inverse compressibility χ^{-1} versus reduced density ρ^*, obtained using Eq.(14) at successive orders, are shown in Fig.6. Here, the left panel (A) is for $T^* = 1.45$ (in one-phase region) while the right panel (B) corresponds to $T^* = 1.15$ (in spinodal region). Note that the graphs depict partial sums of the series terms. Thus, χ^{-1} obtained using $c_0(r/\sigma)$ (curve-0), $c_0(r/\sigma) + c_1(r/\sigma)$ (curve-1), $c_0(r/\sigma) + c_1(r/\sigma) + (1/2)c_2(r/\sigma)$ (curve-2), etc., and finally $c(r/\sigma)$ (curve-6) are shown in the panels. Just like in the case of correlation functions, the main contribution of attractive potential comes up at first order correction, although it over corrects a bit. Both panels show convergence of the curves to well defined profiles of χ^{-1}. It is positive in the entire range of ρ^* for $T^* = 1.45$, as expected. But for $T^* = 1.15$, there is a region of ρ^* where χ^{-1} is negative. Pressure βP along the isotherm, obtained via integration over density (starting from $\rho^* = 0$), shows the familiar van der Waals loop. Thus the thermodynamic properties obtained via CPE, although much more accurate, are similar to those of any first order mean field theory.

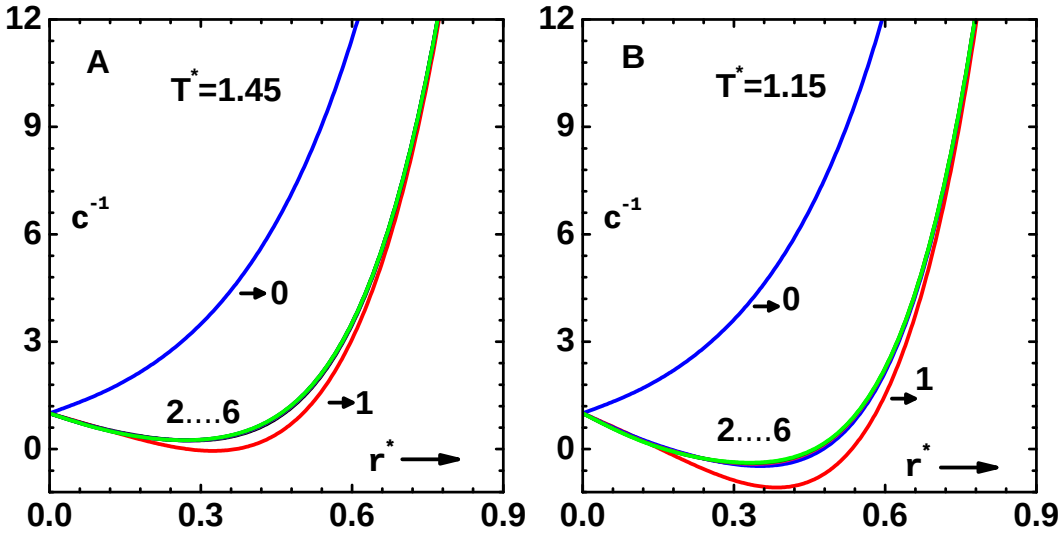

Figure 6. Graphs show inverse compressibility χ^{-1} versus reduced density ρ^* obtained at successive orders of series expansion. Thus, χ^{-1} calculated with just $c_0(r/\sigma)$ (curve-0), $c_0(r/\sigma) + c_1(r/\sigma)$ (curve-1), $c_0(r/\sigma) + c_1(r/\sigma) + (1/2)c_2(r/\sigma)$ (curve-2), etc., and finally $c(r/\sigma)$ (curve-6) are shown. (**A**) Graphs for reduced temperature $T^* = 1.45$ in one-phase region. (**B**) Similarly, for $T^* = 1.15$ in the spinodal region.

There is an issue related to the occurrence of negative compressibility (at any phase point) because it implies, by continuity requirements, that $1 - \rho\bar{c}(k_0)$ would vanish at some positive value k_0. This is so because $\bar{c}(k)$ should tend to zero for sufficiently large k. Then, the transforms $\bar{y}(k_0)$ (see Eq.(**??**)) and consequently $\bar{h}(k)$ would diverge at k_0. Thus, negative compressibility at any phase point implies a singularity in the Fourier transform $\bar{h}(k)$ [8]. Taylor's series expansions in CPE do not converge to this singular solution, in fact, numerical results provided above indicate that they converge to a different solution. This is plausible as multiple solutions are known to exist in the two-phase region.

The correlation functions and thermodynamic properties in the spinodal region, although converge to well defined profiles, are nonphysical, as they generate negative compressibility and van der Waals's loop in pressure. Their utility in computing phase diagram (via thermodynamic conditions or Maxwell's construction) needs to be evaluated by comparing the results with those from independent methods (see below). In any case, weighted averaging of contributions of gas and liquid phases is needed to obtain physically acceptable properties.

It is important to check convergence of CPE results on an isotherm close to the critical point. This is done in Fig.7A, which shows χ^{-1} versus ρ^* (curve-1) on isotherm for $T^* = 1.33$. Results of independent computations (symbols) [10] are also shown. The latter results are for identical model, but are based on Newton's method applied to the full potential, together with very careful strategies to mark out the spinodal region. Reduced temperature $T^* = 1.33$ is just above the critical temperature $T_c^* = 1.326$, obtained via CPE, as discussed next. The agreement between the two sets of results is quite good, thereby demonstrating convergence of χ^{-1} profile in CPE even close to the critical point. The insert figure shows pressure βP (curve-1) and chemical potential $\beta\mu$ (curve-2) obtained via the compressibility route, i.e., by integrating χ^{-1} profile (see Eq.(15)) from zero to ρ^*. Nearly flat regions in these graphs, over a range of ρ^*, show the closeness of the isotherm to the critical isotherm.

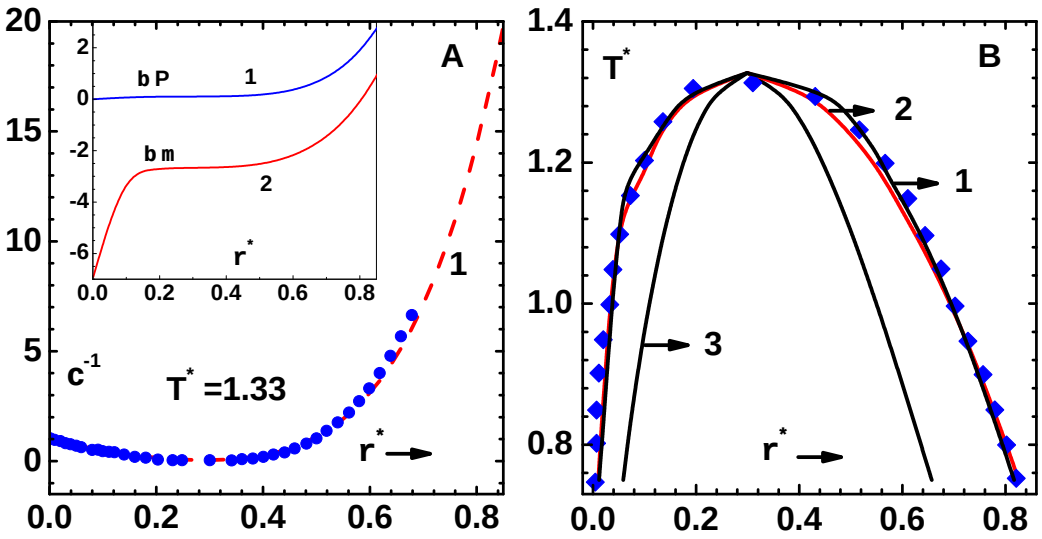

Figure 7. (**A**) Comparison of χ^{-1} versus ρ^* obtained using CPE (curve-1) and independent computations (symbols) [10] on the isotherm for $T^* = 1.33$, which is just above the critical temperature. The inset graphs show pressure βP (curve-1) and chemical potential $\beta\mu$ (curve-2) (both obtained via compressibility route) on the same isotherm. (**B**) Comparison of co-existence lines, obtained with CPE, using thermodynamic conditions (curve-1) and Maxwell's construction (curve-2), with simulation results (symbols) [29]. The spinodal lines (curve-3) on gaseous and liquid sides are also shown.

Next, the phase diagram (co-existence curves) of the LJ system obtained via CPE is compared against simulation data (symbols) [29]. Two schemes are used for this purpose: (i) thermodynamic conditions (i.e., $P_L = P_G$ and $\mu_L = \mu_G$ discussed earlier) via free energy route (curve-1) and (ii) Maxwell's construction via compressibility route (curve-2). Note that the first scheme (see Eq.(13)) is not dependent on the results within the spinodal region. The second scheme uses results in the negative compressibility region for getting P and its volume-integral on the liquid side of the phase-plane. The good agreement between the two schemes show that χ^{-1} profiles in the spinodal region are accurate interpolations between those in the gas and liquid sides. There are only slight differences between the results of the two schemes, along the liquid branch near the transition point. The simulation data agree better with the results of the former. Critical point parameters are also obtained using two methods: (i) solving the defining equations, $\partial_v P = 0$ and $\partial_v^2 P = 0$, and (ii) extrapolating values of χ^{-1}_{min} (over density) to zero, on different isotherms in the one phase region. These methods provide almost identical critical point parameters: $\rho_c\sigma^3 = 0.299$ [0.312], $k_B T_c/\epsilon = 1.326$ [1.316] and $P_c\sigma^3/\epsilon = 0.102$ [0.127], which compare well with simulation data given in square brackets. The spinodal lines on the gas and liquid sides (curve-3) are also shown in the figure.

5.1. Generalized LJ(n,m) potentials

The LJ potential is generalized to LJ(n, m) family of potentials, with arbitrary power law exponents n and m, in the expression:

$$U(r) = \frac{m\,\epsilon}{n-m}\left(\frac{n}{m}\right)^{n/(n-m)}\left[\left(\frac{\sigma}{r}\right)^n - \left(\frac{\sigma}{r}\right)^m\right]. \tag{27}$$

The pre-factor is chosen so that potential depth is ϵ for all n and m. Varying the exponent n, while keeping $m = 6$, generates a family of potentials, also called Mie (n,6) potentials. The effective potential-range is altered on varying n; larger n yielding narrow and smaller n broad potentials. These

potentials have applications in modeling systems in soft matter physics, and have been investigated via molecular dynamics simulations [30] and integral equation theory [10].

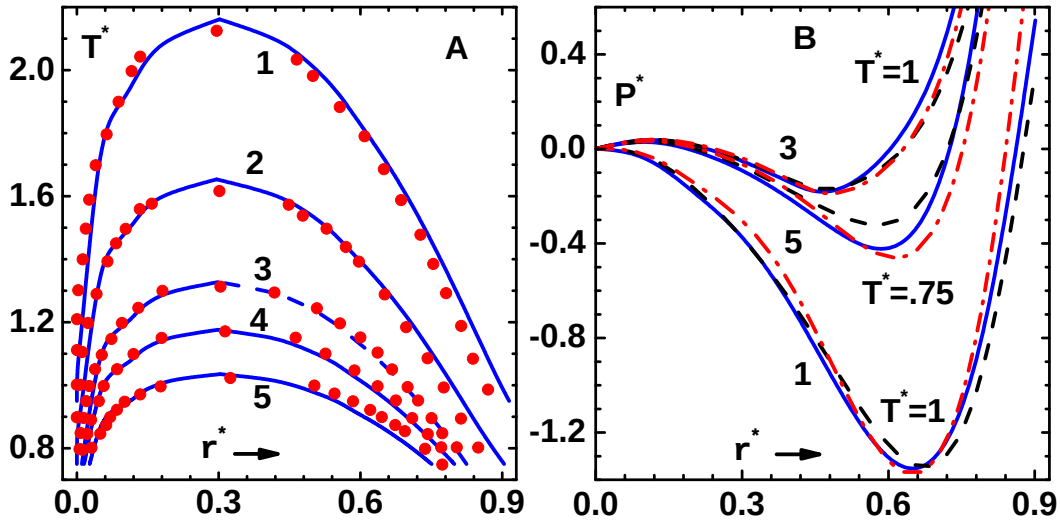

Figure 8. (**A**) Comparison of co-existence lines, obtained with CPE, for potentials: LJ(7,6) (curve-1), LJ(9,6) (curve-2), LJ(12,6) (curve-3), LJ(15,6) (curve-4) and LJ(20,6) (curve-5), with simulation data (symbols) [30]. (**B**) Reduced isotherms for LJ(7,6) (curve-1) using virial (solid line), compressibility (dashed line) and free energy (dash-dot line) routes corresponding to $T^* = 1$. Other sets of graphs are for LJ(12,6) (curve-3) at $T^* = 1$ and LJ(20,6) (curve-5) at $T^* = 0.75$

Phase diagrams, obtained with CPE, are compared with simulation data (symbols) [30] in Fig.8A for potentials LJ(7,6) (curve-1), LJ(9,6) (curve-2), LJ(12,6) (curve-3), LJ(15,6) (curve-4) and LJ(20,6) (curve-5). These results are obtained via the compressibility route mentioned earlier. Perhaps, results obtained via CPE offer better comparison with simulation data than that obtained using Newton's method applied to full potential [10]. It is also possible in CPE to approach the critical point closer on both branches. The gaseous branches and critical points compare well for all cases. However, there are differences on the liquid side for $n = 7$, $n = 9$ and $n = 20$ cases. In fact, CPE results lie above simulation data for softer cases (smaller n) where as the trend is just opposite for harder (larger n) cases. Results agree quite well on both branches for intermediate values $n = 12$ and $n = 15$. A ppssible reason for this is analyzed in Fig.8B, which show reduced isotherms for LJ(7,6) (curve-1) obtained via the virial (solid line), compressibility (dashed line) and free energy (dash-dot line) routes for $T^* = 1$. Similar sets of graphs for potentials LJ(12,6) (curve-3) at $T^* = 1$ and LJ(20,6) (curve-5) at $T^* = 0.75$ are also shown in the panel. There results indicate that the bridge function [18] provides much better thermodynamic consistency for the intermediate cases ($n = 12$ and 15) while important deviations are noted for softer and harder potentials. This might explain the differences in the phase diagrams on the liquid branch for the latter cases.

6. Summary

The main aim in this paper is to analyze convergence of CPE for solving the OZE. After providing brief details of CPE, its convergence is evaluated first for the two analytically solvable AHS and MSA models. Both these models show the emergence of a 'no-real-solution-region' in the two phase domain of the phase plane. The CPE, which is based on series expansions around the correlation functions

of the (repulsive) reference potential, always generate real solutions. Hence it does not converge in regions where there are only complex solutions. In fact, convergence is slower in the neighborhood of the 'no-real-solution-region'. However, this does not affect computation of phase diagram of AHS model because it completely contains the 'no-real-solution-region'. Convergence issue is evaluated in details for the LJ system modeled using an accurate density-dependent bridge function and 7-th order solutions. Spatial profiles of correlation functions, corresponding to phase points above as well as below the critical point, are found to approach well defined functions. Similarly, density-profiles of inverse compressibility (above, below and close to critical point) also converge to appropriate functions. The phase diagrams of LJ model obtained via two independent schemes using the free energy and compressibilty routes agree well, and also with simulation data. The whole procedure is also evaluated with reference to simulation data on the generalized LJ(n,6) family of potentials. These potentials with variable ranges important applications in soft condensed matter. The main conclusion of this paper is that CPE provides a practical approach to evaluate thermodynamic proprieties of one component fluids described using general pair-potentials.

References

1. Hansen, J.P.; McDonald, I.R. Theory of Simple Liquids (Forth Edition) *Academic Press, Cambridge.* **2013**.
2. Martynov, G. A. The problem of phase transitions in statistical mechanics *Physics-Uspekhi* **1999**, *42*, 517.
3. Sarkisov, G. N. Approximate equations of the theory of liquids in the statistical thermodynamics of classical liquid systems *Physics-Uspekhi* **1999**, *42*, 545.
4. Kelley, C. T. Solving nonlinear equations with Newton's method, Fundamentals of Algorithms *SIAM, Philadelphia* **2003**.
5. Zerah, G. An efficient Newton's method for numerical solution of fluid integral equations *J. Comp. Phys.* **1985**, *61*, 280.
6. Watts, R. O. Percus-Yevic equation applied to a Lennard-Jones fluid *J. Chem. Phys.* **1968**, *48*, 50.
7. Baxter, R. O. Percus-Yevick equation of hard spheres with surface adhesion *J. Chem. Phys.* **1968** , *49*, 2770.
8. Sarkisov, G. N.; Lomba, E. The gas-liquid phase transition singularities in the framework of the liquid-state integral equation formalism *J. Chem. Phys.* **2005**, *122*, 214504.
9. Cummings, P. T.; Smith, E. R. Liquid-gas transition for hard spheres with attractive Yukawa tail interactions *Chem. Phys.* **1979**, *42*, 341.
10. Charpentier, I.; Jakse, N. Phase diagram of complex fluids using an efficient integral equation method *J. Chem. Phys.* **2005**, *123*, 204910.
11. Solana, J. R. Perturbation theories for thermodynamic properties of fluids and solids *CRC Press, New York.* **2013**
12. Zhou, S. ; Solana, J. R. Progress in the perturbation approach in fluid and fluid-related theories *Chem. Rev.* **2009**, *109*, 2829.
13. Tang, Y. ; Lu, B.C.Y. A new solution of the Ornstein-Zernike equation from perturbation theory *J. Chem. Phys.* **1993**, *99*, 9828.
14. Sai Venkata Ramana, A. ; Menon, S. V. G. Coupling-parameter expansion in thermodynamic perturbation theory *Phys. Rev.* **2013**, *E 87*, 022101.
15. Weeks, J.D. ; Chandler, D. ; Andersen, H.C. Role of Repulsive Forces in Determining the Equilibrium Structure of Simple Liquids *J. Chem. Phys.* **1971**, *54*, 5237.
16. Menon, S. V. G. Scaling of phase diagram and critical point parameters in liquid-vapor phase transition of metallic fluids *Condensed Matter* **2021** , *6*, 1.
17. Menon, S. V. G. ; Bishnupriya Nayak, An equation of state for metals at high temperature and pressure in compressed and expanded volume regions *Condensed Matter* **2019** , *4*, 71.
18. Sarkisov, G. N. Structure of simple fluid in the vicinity of the critical point: approximate integral equation theory of liquids *J. Chem. Phys.* **2003**, *119*, 373.
19. Kelley, C. T. ; Pettitt, B.M. A fast solver for Ornstein-Zernike equations *J. Comp. Phys.* **2004**, *197*, 491.
20. Lado, F. Perturbation correction for the free energy and structure of simple fluids *Phys. Rev.* **1973**, *A 8*, 2548.

21. Barboy, B. On a representation of the equation of state of fluids in terms of the adhesive hard-sphere model*J. Chem. Phys.* **1974**, *61*, 3194.
22. Baxter, R. J. Ornstein-Zernike relation for a disordered fluid *Aust. J. Phys.* **1968** , *21*, 563.
23. Menon, S. V. G. ; Manohar, C. ; Srinivasa Rao, K. A new interpretation of the sticky hard sphere model *J. Chem. Phys.* **1991** , *95*, 9188.
24. Waisman, E. The radial distribution function for a fluid of hard spheres at high densities Mean spherical integral equation approach *Mol. Phys.* **1973** , *25*, 45.
25. Peplow, A. T. ; Beardmore, R. E. ; Bresme, F. Algorithms for the computation of solutions of Ornstein-Zernike Equation *Phys. Rev.* **2006**, *E 74*, 046705.
26. Tikhonov, D. A. ; Sarkisov, G. N. Singularities of solution of the Ornstein-Zernike Equation within the gas-liquid transition region *Russian J. Phys. Chem.* **2000**, *74*, 470.
27. Gubbins, K.E. ; Smith, W.R. ; Tham, M.K. ; Tiepel, E.W. perturbation theory for the radial distribution function *Mol. Phys.* **1971** , *22*, 1089.
28. Heyes, D.M. ; Okumura, H. Equation of state and structural properties of Weeks-Chyandler-Andersen fluid *J. Chem. Phys.* **2006** , *124*, 164507.
29. Johnson, J. K. ; Zollweg, J.A. ; Gubbins, K. E. The Lennard-Jones equation of state revisited *Mol. Phys.* **1993**, *78*, 591.
30. Okumura, H. ; Yonezawa, F. Liquid–vapor coexistence curves of several inter-atomic model potentials *J. Chem. Phys.* **2000** , *113*, 9162.